Axial coordination tuning Fe single-atom catalysts for boosting H_2O_2 activation

Haoyang Fu [a,b,1], Jiaqi Wei [b,1], Guoliang Chen [b], Minkai Xu [a], Jiyuan Liu [b], Jianghong Zhang [b], Ke Li [c], Qianyu Xu [a], Yunjie Zou [a], Wei-xian Zhang [a], Shibo Xi [d], Xiaodong Chen [b], Shuzhou Li [b,**], Lan Ling [a,*]

[a] State Key Laboratory for Pollution Control and Resource Reuse, College of Environmental Science and Engineering, Tongji University, Shanghai 200092, China
[b] School of Materials Science and Engineering, Nanyang Technological University, 50 Nanyang Avenue, Singapore 639798, Singapore
[c] Institute of Materials Research and Engineering, Agency for Science, Technology and Research, 138634, Singapore
[d] Institute of Chemical and Engineering Sciences, Agency for Science, Technology and Research, 1 Pesek Road, Jurong Island, Singapore 627833, Singapore

ARTICLE INFO

ABSTRACT

Precisely regulating the coordination microenvironment of single-atom catalysts (SACs) to achieve enhanced reactivity is significant and desired but still in its infancy. Herein, a coordination-tuned and pyrolysis-free strategy is reported for the fabrication of a Fenton-like SAC containing the axial five-coordinated configuration (Fe–N5). The N species on the N-doped graphene act as anchoring points for iron phthalocyanine (a typical Fe–N4 complex) to obtain isolated Fe–N5 sites, which significantly modulates the electronic state of Fe atoms and lowers the H_2O_2 activation barrier for •OH production. Moreover, the enriched pyridinic N serve as contaminant adsorption sites shortening •OH diffusion distance, establishing a dual-site reaction mechanism with Fe–N5 sites. As such, the Fe–N5 catalyst exhibits exceptional Fenton activity towards catalytic oxidation of phenol (k = 0.180 min^{-1}). Our work unravels the dependence of Fenton activity on the single-atom coordination environment and provides a platform for precise engineering of SACs.

1. Introduction

Advanced oxidation processes (AOPs) are considered as promising approaches to obtain reactive oxygen species (ROS), which serve as strong oxidants in wastewater treatment [1], soil remediation [2], cancer therapy [3,4], etc. The Fenton process is one of the most efficient AOPs that can generate highly active hydroxyl radicals (•OH) from the reaction of Fe^{2+} and hydrogen peroxide (H_2O_2) under ambient conditions [5]. However, a narrow pH range (3−4) for such homogeneous reaction as well as accumulation of ferric hydroxide sludge at high pH environments limit its large-scale applications, especially for cleaning up recalcitrant organic contaminants in solution [6]. Heterogeneous Fenton-like catalysts in different types, including Fe-containing minerals [7], Fe nanoparticles [8], and other Fe supported catalysts [9,10], can extend the working pH range from acidic to alkaline, and be recovered

without ferric hydroxide precipitation. Nevertheless, the efficient utilization of Fe atoms in heterogeneous Fenton-like catalysts remains a pivotal challenge ahead of their practical applications.

The discovery of Fe single-atom catalysts (SACs) bridges the gap between heterogeneous and homogeneous Fenton catalysis. Atomically dispersed Fe single-sites in SACs are often under the coordination of N/C atoms on a carrier, which exposes the active center almost completely to reactants and intermediates, thus obtaining near 100 % utilization of Fe atoms to activate H_2O_2 for organic pollutants degradation [11–16]. The coordination configuration of Fe single-atom sites has been demonstrated to play a decisive role in determining the catalytic properties by modifying the scaffold such as changing the coordination number of Fe atoms, doping with heteroatoms (N, P, S, etc.), and tuning the compressive strain [17–20]. Fe macrocycles, such as Fe porphyrins and phthalocyanines, are the precursors most widely used to prepare the

---

Fenton-like catalysts [21,22]. To date, however, limited progress has been made in improving their Fenton activity and durability. In particular, the obtained catalysts have been demonstrated a long-time degradation in performance due to the demetalation of Fe macrocycles in solution [23,24]. Although the high-temperature pyrolysis strategy was applied to modify the geometric and electronic structure of metal macrocycles to overcome existing drawbacks of catalysts, the serious destruction of the precursor by this strategy results in nearly uncontrollable and complex coordination environments for single-atom metals, making it tough to unravel the relationship between local architecture and catalytic activity [25–27]. As such, achieving a rational structural design and geometric engineering of catalytic single-atom sites to control their catalysis performances, as well as exploring the correlation between the catalyst structure and the reactivity, is highly desirable, yet challenging till now.

Herein, we report a moderate and facile axial coordination strategy to obtain effective Fenton-like catalyst with precisely designed isloated Fe–N$_5$ catalytic sites. The strategy utilizes N-doped graphene (NG) with N atoms as the anchoring site for iron phthalocyanine molecules ($(C_8H_4N_2)_4Fe$, FePc), resulting in well-preserved structure of Fe–N$_5$ sites on NG and therefore successful modulation of the axial coordination of Fe single-atoms. The Fe–N$_5$ sites dispersed N-doped graphene (FeN$_5$/NG) exhibits superior Fenton-like degradation of phenol (a typical organic contaminant), a degradation rate constant of 0.180 min^{-1}, which exceeded most of the state-of-the-art Fenton-like catalysts. Our approach combining experiments and numerical simulations demonstrate the role of the pyridinic N site on NG is to adsorb phenol molecules, with the Fe-N$_5$ site catalyzing •OH formation. Moreover, quantum calculations reveal that the Fe–N$_5$ site provides less charge to 2OH* intermediate but more charge to OH* intermediate compared to the Fe–N$_4$ site, giving rise to a lower energy barrier for •OH generation to improve the catalytic performance. This work presents a paradigm for axial coordination tuning of SACs and establishes both theoretical and experimental foundations of accurate structure–activity relationships for the construction of efficient Fenton catalysis.

2. Materials and methods

2.1. Synthesis of FeN$_5$/NG catalyst

The fabrication of FeN$_5$/NG was started with the modification of graphene oxide (GO). Briefly, 1.5 mL of ammonia (28 wt%) and 100 μL of hydrazine hydrate (80 wt%) were mixed with 400 mL of GO aqueous dispersion (0.4 g/L) into a 1 L of three-neck flask. The resulting mixture was put in an oil bath and heated at 95 °C for 60 min to form the reduced graphene oxide (rGO). The as-synthesized rGO was then annealed at 600 °C for 240 min in a quartz tube furnace under a 15 vol% Ar/NH$_3$ gas mixture. The NG was finally obtained after cooling to 25 °C. The FeN$_5$/NG catalyst was synthesized by admixing 100 mg of NG and 40 mg of FePc in 10 mL of anaerobic deionized water, with magnetic stirring for 10 min, followed by freeze-drying for 60 min. The FeN$_5$/NG catalyst was washed with water and ethanol several times to remove uncoordinated FePc before use. For comparative studies, the Fe–N$_4$ sites dispersed on the reduced graphene oxide (FeN$_4$/G) and Fe–N$_4$ sites dispersed on the NG (FeN$_4$/NG) were also synthesized in the similar way, except that the modification of reduced graphene oxide in FeN$_4$/G was under the Ar environment and the heating temperature was set to 600 °C during anchor of Fe single atoms for FeN$_4$/NG. Moreover, a series of catalysts with different content of pyridinic N species were prepared by adding a pyrolysis process (modulation of the pyrolysis temperature from 500° to 900 °C) between the synthesis of NG and the single-atom anchoring process for the investigation of correlation between phenol adsorption efficiency and pyridinic N content. Increasing the pyrolysis temperature from 500° to 900 °C enables a significant change in the N distribution of the catalyst without obvious loss of N content (Table S1). Samples obtained after pyrolyzing at 500, 700, and 900 °C were denoted as FeN$_5$/

NG-500, FeN$_5$/NG-700, and FeN$_5$/NG-900, respectively, and some physicochemical properties of FeN$_5$/NG-500, FeN$_5$/NG-700, and FeN$_5$/NG-900 are provided in Table S2.

2.2. Analysis and characterization

The powder X-ray powder diffraction (PXRD) spectra were obtained on a powder X-ray diffractometer (Bruker D8 Advance; Bruker AXS, German) with a high-power Cu Kα (40 kV, 40 mA, λ = 1.54178 Å) radiation source. Scanning/transmission electron microscopy (S/TEM) was measured using Cs-corrected FEI Titan™ G^2 60–300 instrument (FEI Ltd., Hillsboro, USA) operating at 300 kV with energy dispersive X-ray spectroscopy (EDS) for analysis of catalyst composition. X-ray photoelectron spectroscopy (XPS) analyses of samples were conducted using ESCALAB 250Xi (Thermo Fisher Scientific, USA) with a monochromatic K-Alpha source (1486.6 eV). An inductively coupled plasma atomic emission spectroscopy (ICP-OES, Optima2000, PerkinElmer, USA) was used to measure the elemental compositions. The X-ray absorption structure (XAS) was performed at the X-ray Absorption Fine Structure for Catalysis (XAFCA) beamline of Singapore Synchrotron Light Source (SSLS) center with stored electron energy of 2.2 GeV using transmission mode [28].

2.3. Computation methods

All spin-polarized calculations involving density functional theory (DFT) in the present work are calculated by the Vienna Ab initio Simulation Package (VASP) program [29]. The ion-electron interaction is described by the Projector augmented wave (PAW) pseudopotential method [30]. The plane-wave basis set is cut off at 600 eV and 450 eV for lattice optimization and geometry optimization of adsorption intermediate, respectively. Generalized gradient approximation (GGA) with the revised Perdew-Burke-Ernzerhof (PBE) functional was applied to determine the exchange-correlation energy [31]. The energy and force convergence thresholds at which all atoms are released during the structure optimization iteration are set to be 10^{-4} eV and 0.03 eV/ Å. FeN$_4$C$_{20}$ porphyrin structures terminated by hydrogen atoms were adopted to construct the FeN$_4$ model. The NC carrier was simulated by constructing three carbon atoms substituted with nitrogen atoms on a periodic 10 × 10 × 1 graphene plane, and the FeN$_5$ model is constructed by linking the FeN$_4$C$_{20}$ porphyrin group to the modified graphene plane with a Fe-N bond. A (3 ×3 ×l) K-point grid is employed for structural optimization and electronic structural calculations. Moreover, DFT-D3 method is adopted to accurately describe the van der Waals force interaction between catalysts and adsorbates [32]. FeN$_4$, FeN$_5$, and other molecules such as H$_2$O$_2$ and H$_2$ are put in the same box. The vacuum layer thickness of 20 Å is set in the z-direction to avoid the influence of the interaction between adjacent periodic structures. The solvent effects were accounted by using an implicit solvation model as implemented in the DFT code VASP [33]. The adsorption energy E$_{ad}$ is defined as $E_{ad} = E_{sa} - E_{cs} - E_{as}$, where E_{sa}, E_{cs}, and E_{as} is the total energy of substrate with adsorbates, the total energy of the clean substrate, and the total energy of adsorption species, respectively. Fe K edge theoretical XANES spectra of the DFT optimized structures were simulated using the finite difference method (FDM), which was implemented within the Finite Difference Method Near Edge Scattering (FDMNES) package developed by Joly [34]. Broadening contributions from the core–hole lifetime, the inelastic plasmon interaction with photoelectron, the resolution of the beamline, and the Fermi energy was accounted for using an arctangent convolution [35].

2.4. Examination of catalysts

Batch experiments were performed to test the Fenton activities of FeN$_5$/NG catalyst. The stock solution of phenol (200 mg/L) was prepared by dissolving 200 mg phenol in 1 L of anaerobic deionized water.

The phenol removal efficiency in the FeN$_5$/NG, FeN$_4$/NG+H$_2$O$_2$, FeN$_5$/NG+H$_2$O$_2$, NG+H$_2$O$_2$, and homogeneous Fenton (Fe^{2+}+H$_2$O$_2$) systems are compared. Typically, 2 mg of catalysts were added into 20 mL of a 20 mg/L phenol solution for 30 min to reach the adsorption-desorption equilibrium in the heterogeneous system. The Fenton-like reaction was initiated by adding 10 mmol/L of H$_2$O$_2$ aqueous solution. The same amount of Fe^{2+} (Fe^{2+} used in the experiment is FeSO$_4$) as in FeN$_5$/NG was added to the homogeneous system. The effect of pH/ H$_2$O$_2$ dosage on phenol degradation was evaluated by mixing 20 mg FeN$_5$/NG with 200 mL phenol solution (20 mg/L) with different initial pH values/ added H$_2$O$_2$ dosages. A 5-mL suspension was taken at fixed time intervals for each batch of the experiment and then filtered to measure phenol concentration. 0.5 mL of isopropanol (IPA) was added after the samples were taken in all batch experiments to prevent further reaction of the ROS with phenol in solution.Ten cycling tests were carried out to investigate the reusability of the FeN$_5$/NG for the degradation of phenol. The recycled catalyst was treated with UV irradiation before the next Fenton-like reaction.

The concentration of phenol was monitored by measuring its absorption at 280 nm using an ultraviolet (UV)-visible (vis) spectrophotometer (TU-1901, Beijing Puxi Inc., China). The electron spin resonance (ESR) measurements were performed on a Miniscope MS-5000 ESR spectrometer (Germany), using 5, 5-Dimethyl-1-pyrrolidine-N-oxide (DMPO), dimethyl sulfoxide (DMSO), and 4-Amino-2,2,6,6-tetramethyl-piperidine (TEMP) as the spin-trapping agents for reactive oxygen species (ROS). Radical quenching experiments were carried out to further ascertain the ROS during phenol degradation. IPA (2 mL) and p-benzoquinone (BQ; 15 mg) were chosen as scavenges of •OH and superoxide radical (•O$_2^-$), respectively. The experimental details for ROS capture processes were similar to the batch catalytic experiment. The PMSO and its oxidation product (phenyl methyl sulfone; PMSO$_2$) were identified by an Agilent 1200 high-performance liquid chromatography (HPLC). The cumulative •OH formation in different systems was quantified with the benzoic acid method [36]. 5.87 was used as the conversion factor for the estimation of the cumulative •OH from p-hydroxybenzoic acid (p-HBA). The oxidation product of BA, *p*-HBA, was quantitatively analyzed using a HPLC (Alliance 2695, Waters, USA) with an ACQUITY UPLC@BEH C18 column (2.1 ×50 mm, 1.7 μm, Waters, USA). The mobile phase was a mixture of 0.1% trifluoroacetic acid (TFA) aqueous solution-acetonitrile (60:40, v/v).

3. Results and discussion

3.1. Characterization of FeN$_5$/NG

Fig. 1 illustrates the synthesis protocol of FeN$_5$/NG composites. In this approach, the NG was firstly obtained from rGO annealed at 600 °C in an Ar/NH$_3$ mixture atmosphere. The as-synthesized NG shows highly crumpled sheet-like morphology (Fig. S1, Supporting Information), in

which pyridinic N is strikingly enriched (up to 76.8% of the total nitrogen content for NG; Fig. S2 and Table S3). Afterward, the atomically dispersed metal precursor, FePc, was thoroughly mixed with NG in an aqueous solution and self-assembled with pyridinic N sites in NG via strong π–π interactions. The pyridinic N, as the axial ligand, changes the coordination number of Fe center [37,38], and the atomically dispersed Fe–N$_5$ catalytic site in NG can be obtained after a lyophilization process. Such a pyrolysis-free synthesis approach is moderate without harsh reaction condition, which is crucial to a controlled modulation of coordination environment around the active site.

TEM and SEM images of FeN$_5$/NG show similar morphology of the NG with flakelike layer and wrinkled structure (Fig. 2a and Fig. S3). The interplanar spacing is estimated to be 0.35 nm in the high-resolution TEM (HR-TEM) image, which is attributed to typical (002) basal planes in the graphene layer (Fig. 2a). Raman spectra of both NG and FeN$_5$/NG samples present typical D band (≈ 1318 cm^{-1}) arising from the defects in graphitic lattice and G band (≈ 1580 cm^{-1}) arising from the in-plane vibration of the sp^2 carbon framework (Fig. S4), indicating that NG morphology changes with FePc attached are negligible. The PXRD pattern of FeN$_5$/NG exhibits two wide peaks at $2\theta \approx 24°$ and 44°, corresponding to the (002) and (100) diffraction.

planes of graphite, respectively (Fig. S5), which is further evidenced by the selected area electron diffraction (SAED) pattern (inset of Fig. 2a). No metal-related pattern is detected, ruling out the undesirable formation of metallic particles or aggregates. With aberration-corrected STEM, a large number of atom-scale bright spots that represent single Fe atoms are identified (Fig. 2b). We do not find nanoparticle/nanocluster in the whole region of STEM images which are selected randomly (Fig. S6), in accordance with the PXRD results. The intensity profiles of HAADF image over tracesmarked with orange and green show only one maximum peak, indicating the single atomic state of Fe specie (Fig. 2c). EDS element mappings reveal the homogeneous dispersion of Fe atoms on the NG, with the observed overlapping distribution of Fe, C, and N in Fig. 2d. The mass ratio of Fe on FeN$_5$/NG is determined to be 1.97 wt% by EDS quantitative analysis, being consistent with the overall compositional analysis with ICP-OES (Table S4).

To further identify the local coordination environment of single-atom Fe in FeN$_5$/NG, several spectral analyses were carried out. Wide scan XPS (Fig. S7) shows the occurrence of C, N, O, and Fe elements in FeN$_5$/NG. The C species can be classified into four types: C–C (284.5 eV), C–N (285.4 eV), C–O (286.2 eV), and C=O (288.5 eV). N 1 s XPS spectrum can be deconvoluted into four groups with peaks at 398.2, 399.5, 399.9, and 400.8 eV, assigned to pyridinic N, pyrrolic N, Fe–N$_x$, and graphitic N. The obvious decrease in the ratio of pyridinic N (71.3%) in FeN$_5$/NG compared to NG (76.8%) (Table S3), along with the emergence of Fe–N$_x$ species, indicates the coordination of pyridinic N with Fe atoms in the catalyst. The Fe 2p XPS spectrum of FeN$_5$/NG reveals that Fe^{2+} is the predominant Fe speciation in the sample, as indicated by the relative area ratio of the peaks assigned to Fe^{2+} and Fe^{3+} of 77.9% and

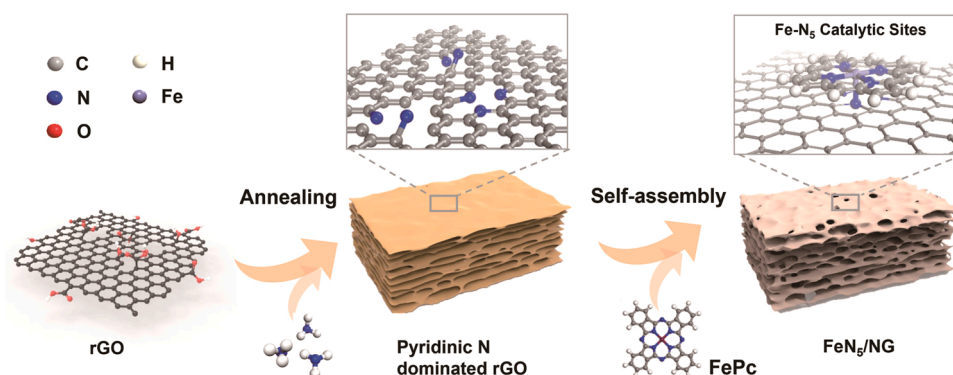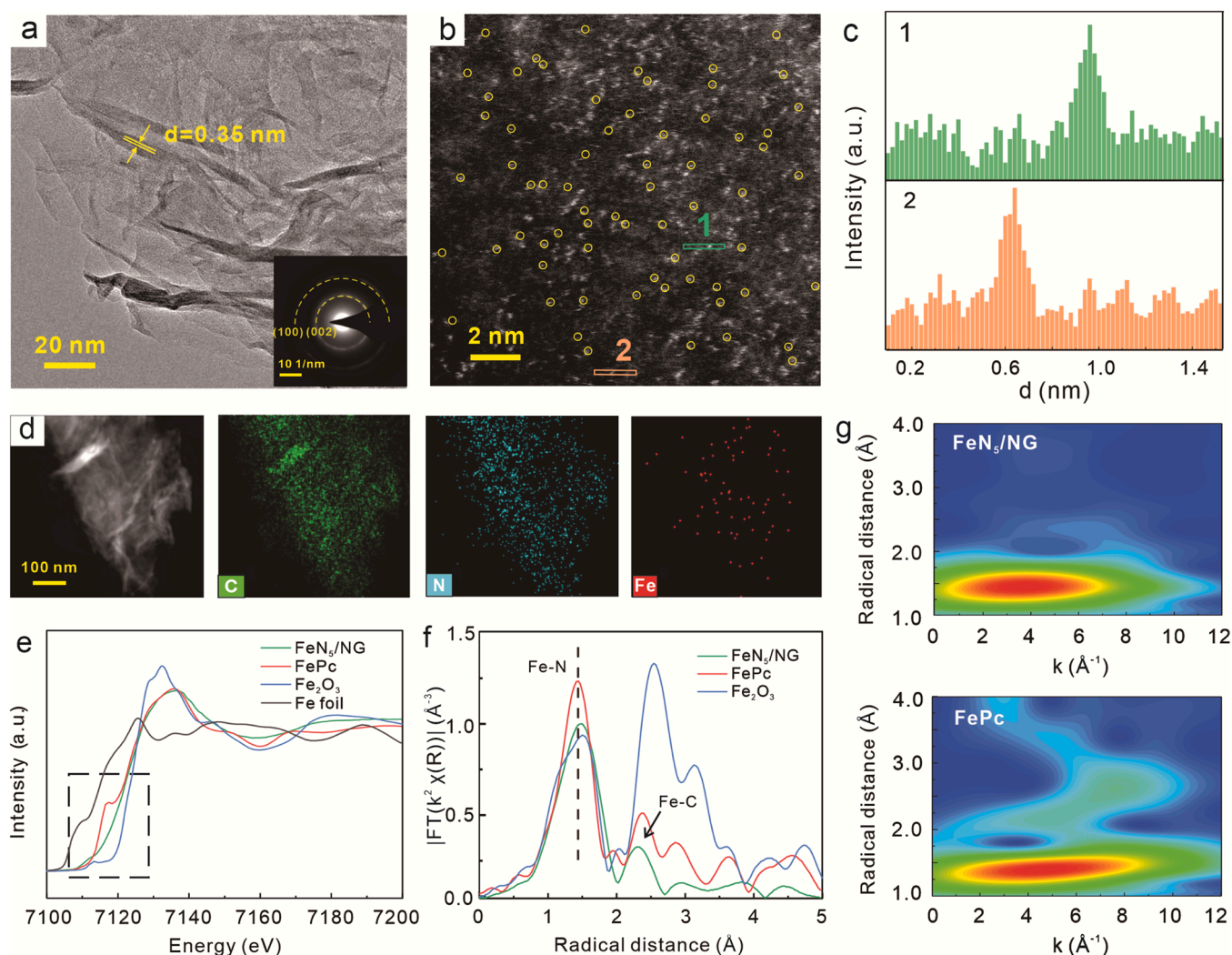**Fig. 1.** Schematic illustration for the synthesis of FeN$_5$/NG.

Fig. 2. Characterization of the FeN$_5$/NG catalyst. a–b) TEM image (a) and HAADF-STEM images (b) of the FeN$_5$/NG catalyst. Inset in (a) is SAED of FeN$_5$/NG catalyst. c) The height profile of Fe single atoms marked in (b). d) EDS mapping (C, N, and Fe) of the FeN$_5$/NG catalyst; e) Fe K-edge XANES spectra of the FeN$_5$/NG, Fe foil, FePc, and Fe$_2$O$_3$. f) FT of the Fe K-edge EXAFS of the FeN$_5$/NG, Fe$_2$O$_3$, and FePc. g) WT analysis of the Fe K-edge EXAFS spectra of the FeN$_5$/NG (top) and FePc (bottom).

22.1%, respectively. The Mössbauer spectroscopy is further conducted to discriminate the coordination structure of Fe atoms. The spectrum of FeN$_5$/NG can be fitted into three doublets (D1-D3). The doublets D2 and D3 are assigned to medium-spin X–Fe^{3+}N$_4$–Y sites (X and Y refer to O or N ligand) and low-spin FePc-like Fe^{2+}N$_4$, respectively [39,40]. D3 can be attributed to N–(Fe^{2+}N$_4$) medium-spin species with a penta-coordinated rhombic monopyramidal structure [40]. The relative absorption area (73.2%) of the second doublet indicates the high content of Fe–N$_5$ catalytic site in FeN$_5$/NG (Fig. S8). Such chemical state of Fe atoms is also verified by XAS. As shown in Fig. 2e, Fe K-edge X-ray absorption near-edge structure (XANES) spectrum of FeN$_5$/NG shows typical features of the blunt white line and weak oscillations for single atom samples. The larger pre-edge shoulder for the square planar structure of FePc disappears, indicating the reconstruction of the coordination structure around Fe atoms. The raising edge of FeN$_5$/NG is located between the ones for FePc and Fe$_2$O$_3$ (marked with the dashed box) with a linearly fitted valance state of + 2.3 (Fig. S9), well consistent with the XPS results. Fourier transformed (FT) Fe K-edge extended X-ray absorption fine structure (EXAFS) shows a scattering peak at ∼ 1.44 Å for FeN$_5$/NG, which represents the Fe−N coordination bonds from both FePc and Fe–NG (Fig. 2f). The bond length for FeN$_5$/NG is slightly larger than the one in FePc, which is due to longer Fe–N coordination bond

and/or the stretched FePc coordination, in accordance with the DFT optimized structure (Fig. 2f and Fig. S10). The characteristic peak representing Fe–C second coordination shell is maintained, indicating the preservation of FePc structure. Together with the faded pre-edge shoulder, this result indicates that FePc is anchored to NG as a molecular complex, and thus should give rise to N-axial coordinated Fe–N$_5$ coordination structure. This is confirmed by both XANES simulations and EXAFS fitting, which provide theoretical spectrum of FeN$_5$/NG with aligned features and well-matched fitting with 5.86 ± 1.48 average Fe–N coordination number, respectively (Fig. S11 and Table S5). The larger first shell Fe coordination number may come from the adsorption of gas molecules in the atmosphere. The wavelet transform (WT) plot of FeN$_5$/NG shows the WT maximum at 3.7 Å^{-1}, corresponding to the Fe–N bonding compared with Fe$_2$O$_3$, Fe foil, and FePc (Fig. 2g and Fig. S12). The insignificant shell of Fe backscatters at ∼2.18 Å corresponding to Fe−Fe coordination suggests that atomic Fe sites are predominantly present without aggregation. In addition, the isolated site dominated with Fe–N$_4$ coordination structure in the FeN$_4$/NG obtained by the pyrolysis process of FeN$_5$/NG is confirmed (Fig. S13, Table S5).

3.2. Fenton-like performance of FeN₅/NG in wastewater treatment

To examine the catalytic role of Fe–N₅ coordination, the Fenton activity of FeN₅/NG is systematically evaluated. Phenol, a typically volatile organic contaminant, is selected as a model contaminant considering its environmental risk. As shown in Fig. 3a, the phenol removal performance of H_2O_2, FeN₅/NG, FeN₄/NG+H_2O_2, FeN₅/NG+H_2O_2, NG+H_2O_2, and conventional homogeneous Fenton (Fe^{2+}+H_2O_2) systems at room temperature are compared. We note that H_2O_2 cannot degrade phenol in 25 min, while phenol removal efficiency for FeN₅/NG only reaches 19.8% in the absence of H_2O_2. Comparatively, the phenol removal efficiency of 99.8% in 25 min is observed for FeN₅/NG after adding H_2O_2. Such a high phenol removal rate of FeN₅/NG far exceeds that of FeN₄/NG catalyst and homogeneous systems, as seen from the first-order reaction rate constant (k_{obs}) of 0.180 min⁻¹ for FeN₅/NG, which is 3.3 and 4.1 times higher than that of FeN₄/NG (0.054 min⁻¹) and homogeneous Fenton process (0.038 min⁻¹), respectively (Fig. 3b). Noting that adsorption is the first and an important step in Fenton-like degradations of contaminants, and high adsorption facilitates the mass transfer of contaminants to the catalysts and driving their oxidative degradation. During this step, FeN₅/NG has similar adsorption behavior to FeN₄/NG, while showing better adsorption capacity and efficiency than FeN₄/G (Fig. S14). Above results highlight the key roles of the N species on NG as the adsorption site for contaminants and axial anchoring site for FePc toward enhanced phenol removal of FeN₅/NG. In addition, FeN₅/NG exhibits more superior Fenton-like performance as comparing with most other state-of-the-art heterogeneous catalysts (Fig. 3c and Table S6). The total organic carbon (TOC) degradation rate within 50 min is over 95 % in the FeN₅/NG+H_2O_2 system (Fig. S15), demonstrating the excellent mineralization ability of FeN₅/NG. Only a minor amount of Fe (< 0.8 mg/L) is leached during the reaction (Fig. S16), which meets the permissible limit of Fe (5 mg/L) according to the Environmental Quality (Sewage and Industrial Effluents) Regulation 1979 [41].

Further experiments are conducted to explore the versatility of FeN₅/NG for phenol removal under different reaction conditions. Fig. 3d reveals the high Fenton activity of FeN₅/NG over a wide pH range, that over 91.2% of phenol can be degraded within 50 min in the pH range of 3–9. Such a broad operating pH for FeN₅/NG is not achievable with most advanced Fenton-like catalysts [42–44]. The removal efficiency is improved from 78.5% to 99.9% in 50 min as the H_2O_2 dosage increased from 2.5 to 20 mmol/L (Fig. S17), due to the participation of H_2O_2 as a precursor in the Fe^{2+}/Fe^{3+} redox cycle, according to the Haber-Weiss mechanism [45]. Recycling experiment was carried out to investigate the stability of FeN₅/NG as a Fenton-like catalyst (Fig. 3e). Although the degradation efficiency slightly decreased as the number of cycles increased, good reusability still remains even after 10 cycles (99.0 % degradation of phenol within 40 min). Moreover, only 9 % of TOC remains after 10 cycles of catalytic reactions, which is much less than that of the conventional homogeneous Fenton system (52 %) (Fig. S18). Noting that the mass loss of FeN₅/NG is less than 0.5 wt% after the 10th cycle (Table S7) and that the microstructure is almost unchanged (Fig. S19), FeN₅/NG shows a high stability in catalyzing Fenton-like process. A slight increase in the relative content of Fe(III) 22.1–26.3 % and a decrease in the relative content of Fe(II) from 77.9 % to 73.7 % are observed after the recycling experiment (Fig. S20), which can be explained that the rate of H_2O_2 with Fe(III) is slower (0.001–0.01 m⁻¹•s⁻¹) than Fe(II) oxidation by H_2O_2 (40 m⁻¹•s⁻¹). The conversion of Fe species in FeN₅/NG might lead to less generation of ROS, which results in the declined activity of FeN₅/NG with increasing cycle.
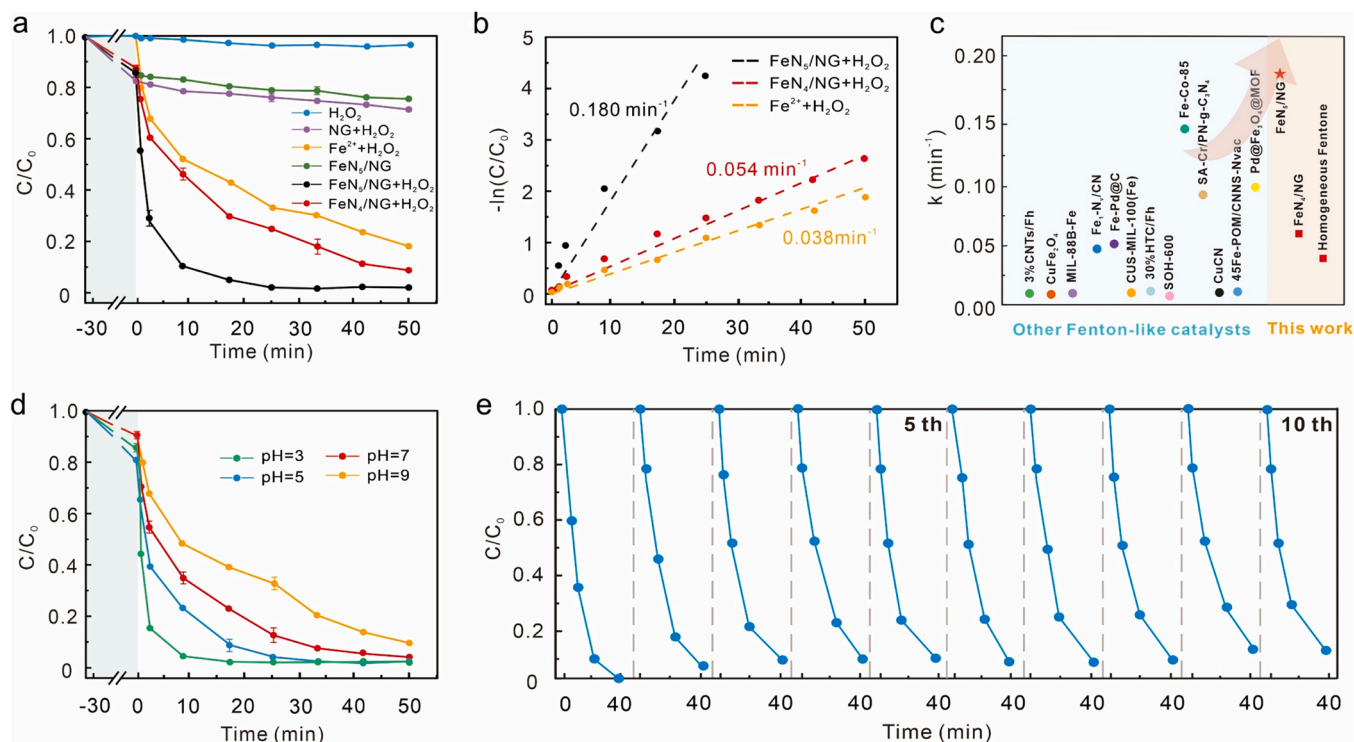

Fig. 3. Fenton activity of FeN₅/NG catalyst. a) Phenol degradation behavior of different catalysts (pH= 4.0 ± 0.2, [Catalyst]= 0.1 g/L, [phenol]= 20 mg/L, [H_2O_2] = 10 mmol/L). b) The corresponding kinetic plots for the phenol degradation with different catalysts. c) Comparison of the kinetics of organic contaminants degradation by recently reported state-of-the-art catalysts. d) The phenol degradation by FeN₅/NG at different pH values. ([Catalyst]=0.1 g/L, [phenol]= 20 mg/L, [H_2O_2]=10 mmol/L). e) Stability of the FeN₅/NG for the degradation of phenol ([phenol]=20 mg/L; The recovered samples were pretreated with UV irradiation only before the Fenton reaction).

3.3. Dual-center mechanism for accelerating phenol degradation

The ROS contributing to phenol degradation are identified by ESR and radical quenching experiments to understand the removal mechanism. As shown in Fig. 4a, the signal of •OH captured by DMPO with four characteristic peaks in a ratio of 1:2:2:1 and the signal of $HO_2•/•O_2^-$ captured by DMSO with characteristic 1:1:1:1 quadruple peak are observed, in the appearance of •OH and $HO_2•/•O_2^-$ in the $FeN_5/NG+H_2O_2$ system. The minor detection of the signals for $^1O_2$ by TEMP spin trapping in both FeN_5/NG-H_2O_2 and FeN_4/NG-H_2O_2 system rules out the possibility of nonradical ROS as the dominant oxidant during phenol degradation (Fig. S21). In addition, almost no $PMSO_2$ was detected in the FeN_5/NG-H_2O_2 system, which implies that the Fe(IV) species is barely involved in the reaction (Fig. S22). The radical quenching experiments utilized IPA for •OH scavenger and BQ as the $HO_2•/•O_2^-$ scavenger. As seen from Fig. 4b, the degradation behavior of phenol by FeN_5/NG slightly decreases in 50 min (down to 77.2%) after addition of BQ, while the deactivation of catalyst is prominent in the presence of IPA (down to 29.7%). This proves that the •OH contributes more than $HO_2•/•O_2^-$ to the decomposition of phenol. With these results, the major ROS generated at the Fe–N_5 active site for phenol oxidation is therefore confirmed to be •OH. Cumulative •OH formed in the $FeN_5/NG+H_2O_2$ system measured with BA as an •OH probe reaches 142.6 µmol/L in 5 min, which is higher than that in FeN_4/NG and homogeneous Fenton systems (Fig. 2f), correspondingly explaining the optimal phenol degradation efficiency of FeN_5/NG. Moreover, the formed p-HBA of FeN_5/NG, to the best of our knowledge, is the highest at the room temperature among other Fenton-like reagents reported so far (Fig. 4c) [46–53], which translates into the excellent oxidative degradation of various other organic contaminants (Fig. 4d).

In general, the adsorption of targat contaminant by Fenton-like catalyst is an important property in determining the degradation performance [54]. In this regard, ascertaining the adsorption-degradation process of phenol by FeN_5/NG is necessary for gaining a deeper insight into the structure-property relationship. N K-edge XAS is performed to monitor the coordination structure evolution of FeN_5/NG during the Fenton-like reaction. As illustrated in Fig. 5a, the initial N

K-edge XANES spectra of FeN_5/NG suspension without phenol exhibits three peaks at around 398.3, 399.2, and 400.8 eV, arising from the electron excitation from N 1 s orbital into antibonding π * states of pyridinic N, pyrrolic N, and graphitic N species, respectively [55]. The order of relative energy positions of these N species are consistent with the XPS results discussed at the beginning. Continuous adsorption of phenol by NG results in the transformation of pyridinic N species on NG, as revealed by the decreased intensity of the pyridinic N peak and the appearance of the new peak at ~402.7 eV after 30 min of adsorption (Fig. 5a). Similar results can be obtained by the XPS characterization, with N 1 s spectra of FeN_5/NG showing a remarkable decrease in the content of pyridinic N and formation of new pyridinic-N^+O^- species (402.2 eV) after adsorption (Fig. 5b) [56]. After the addition of H_2O_2 to degrade phenol, both N K-edge XAS and N 1 s XPS spectra were restored back to the initial state, which indicates that pyridinic N are important phenol adsorption sites for FeN_5/NG. It can be explained that each pyridine N site contains an unpaired electron, which is most readily form a σ bond in this system by pairing with a 2p electron of O atom on phenol and then forms pyridine-N^+O^- species, as supported by DFT calculations showing the highest adsorption energy (E_{ads}; 2.8 eV) for pyridinic N with O atom as compared to other atoms on phenol (Fig. S23). The correlation between the pyridinic N and adsorption ability of FeN_5/NG is further investigated by adjusting the calcination temperature of NG to tailor the amounts of pyridinic N. The relative contents of N species on different catalysts determined by XPS analysis reveal that increasing calcination temperature of NG leads to the conversion of pyridinic N to graphic N, as seen that the ratio of pyridinic N in the catalysts decreases to 37 % after calcination of the NG carrier at 900 °C (Fig. 5c and Fig. S24). The normalized content of pyridinic N on the catalyst has a positive linear relationship with the amount of adsorbed phenol ($R^2 = 0.97$; Fig. 5d). Conversely, no apparent correlation is observed for the normalized content of Fe and pyrrolic N as well as the BET surface area with the phenol adsorption ability (Fig. 5d). Therefore, the pyridinic N on FeN_5/NG should be the primary adsorption site for phenol, and the dual-center mechanism, that is, the pyridinic N site on NC is the phenol adsorption center and the Fe–N_5 site is the H_2O_2 activation center, can be proposed to achieve phenol removal (Fig. 5e). It is worth mentioning
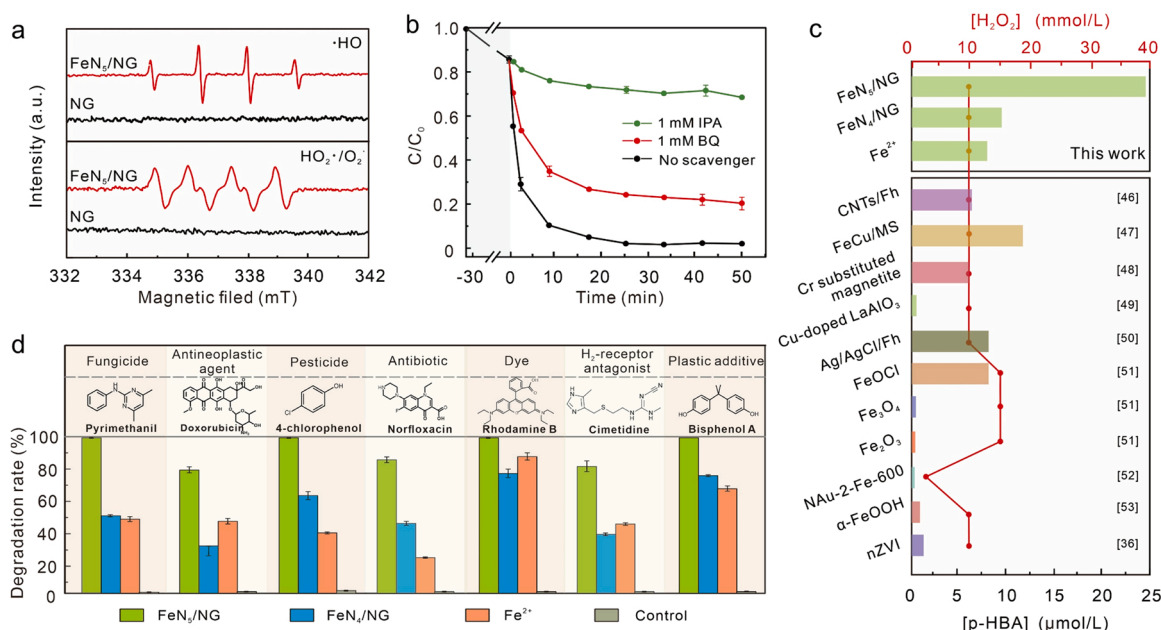
Fig. 4. Generation and detection of ROSs on FeN_5/NG. a) ESR spectra for the detection of •OH (top) in the presence of DMPO and $HO_2•/•O_2^-$ (bottom) in the presence of DMSO. b) Degradation curves of phenol in the presence of different radical scavengers, IPA and BQ ([phenol]=20 mg/L, [IPA]=2 mL, [BQ]=15 mg). c) The concentration of p-HBA in 5 min of different Fenton-like reaction catalysts. d) Degradation of select organic pollutants in $FeN_4/NG+H_2O_2$, $FeN_5/NG+H_2O_2$, conventional homogeneous Fenton ($Fe^{2+}+H_2O_2$), and control (H_2O_2) systems. (pH= 4.0 ± 0.2, [Catalyst]= 0.1 g/L, [organic pollutant] = 20 mg/L, [H_2O_2] = 10 mmol/L, reaction time= 40 min).
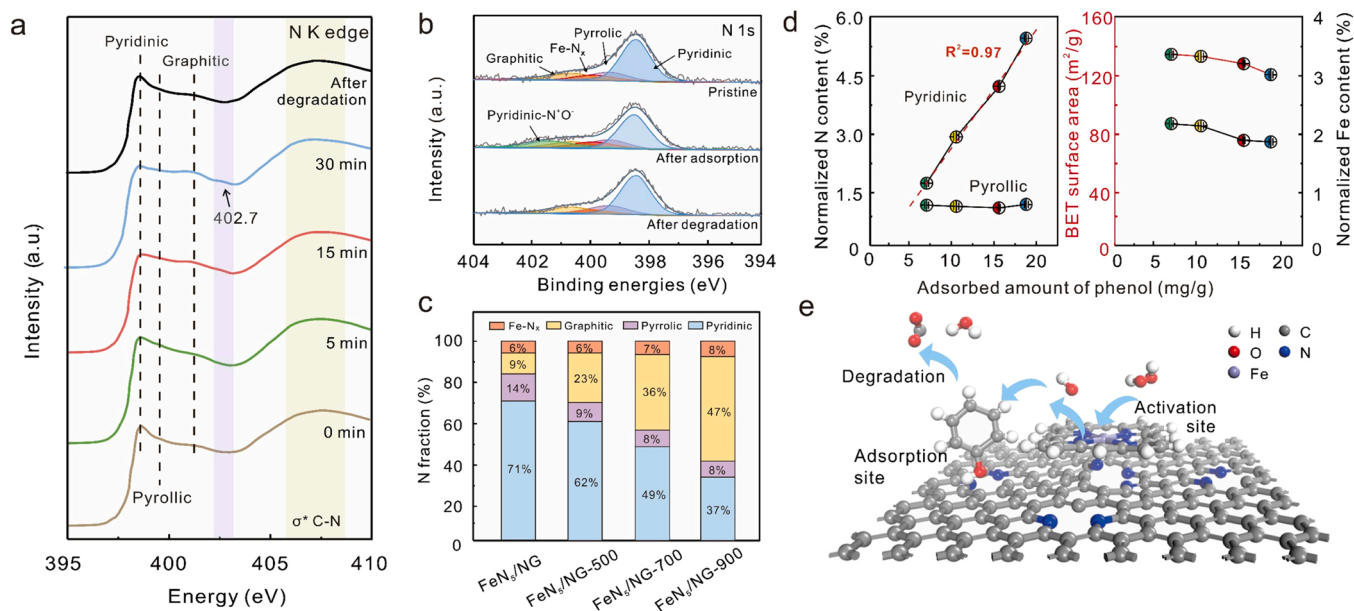
Fig. 5. Phenol adsorption properties of FeN$_5$/NG. a) N K-edge XANES spectra of FeN$_5$/NG at different stages of phenol adsorption. b) N 1 s XPS spectra in FeN$_5$/NG at pristine state, after phenol adsorption, and after phenol degradation. c) The relative contents of different N species in FeN$_5$/NG, FeN$_5$/NG-500, FeN$_5$/NG-700, and FeN$_5$/NG-900. d) The relationship between the adsorbed amount of phenol and the normalized contents of pyrrolic N, pyridinic N, and Fe, as well as the BET surface area. e) Schematic illustration of the dual reaction sites catalytic pollution control mechanisms of FeN$_5$/NG.

that the effective adsorption of phenol onto the pyridinic N site on FeN$_5$/NG results in a decrease in the migration distance of •OH generated from nearby Fe–N$_5$ sites, which could dramatically improve the overall phenol degradation performance.

3.4. Coordination-dependent nanostructure for Fenton activity

To probe the underlying coordination-dependency of Fe single atoms in Fenton catalysis, DFT calculations are utilized to simulate the H$_2$O$_2$ activation process at optimized Fe–N$_x$ (x = 4 or 5) configurations. Noting that the •OH is validated as the primary ROS in this study, a H$_2$O$_2$
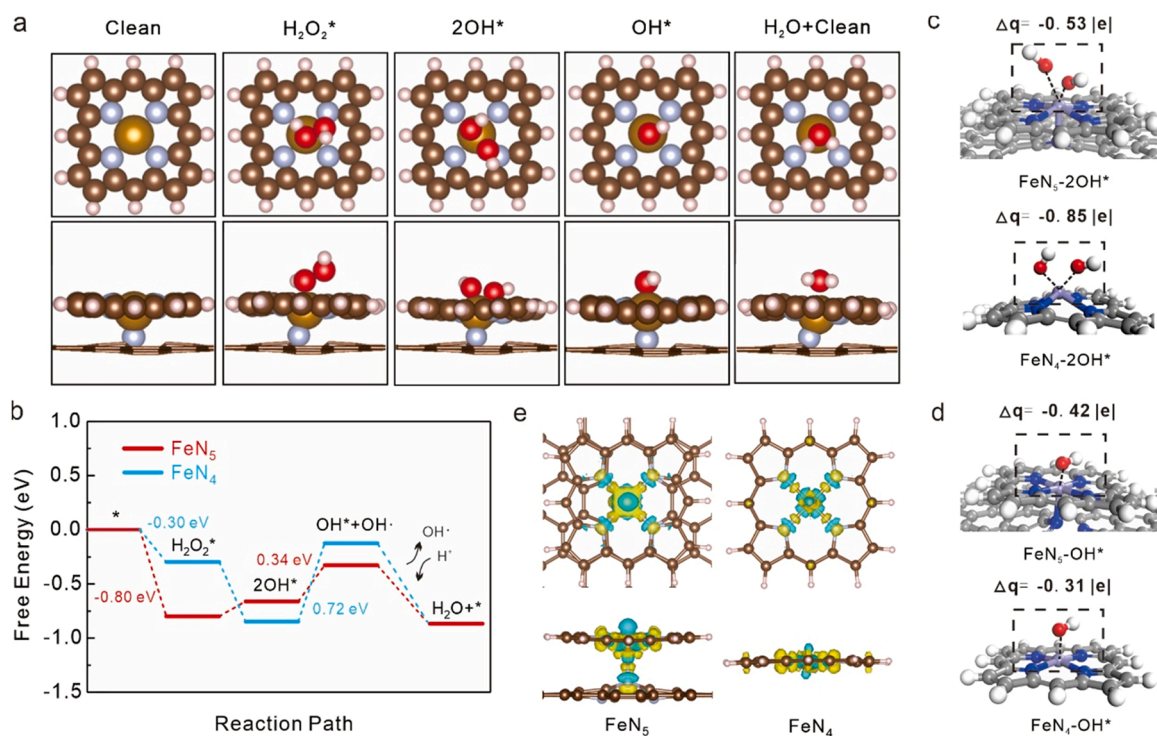
Fig. 6. Fenton activities of coordination-regulated Fe single atoms. a) Proposed Fenton-like reaction process on FeN$_5$/NG under acidic environment. b) Energy diagram of the reaction process for FeN$_5$ and FeN$_4$ models. c-d) Configurations and Bader charge of the adsorption of two OH groups (c) and one OH group (d) on the FeN$_5$/FeN$_4$ models. e) Charge density differences of FeN$_5$ and FeN$_4$ models. The yellow and skyblue regions represent electron accumulation and electron depletion, respectively.

activation pathway under the acidic catalytic milieu is therefore investigated (Fig. 6a). Firstly, the H_2O_2 molecule is adsorbed onto the Fe–N_x active site, which easily undergoes O-O cleavage and then forms two OH* groups. Subsequently, one OH* group desorbs from the adsorbed site to produce an •OH, while the residual OH* can easily reacts with H^+ to form the H_2O product [57]. The Gibbs free energy diagrams and the stepwise atomic structures for intermediates on the Fe–N_x site are summarized (Fig. 6b and Fig. S25, 26). It is noticed that the E_{ads} for H_2O_2 on the Fe–N_4 and Fe–N_5 active sites are 0.30 and 0.80 eV, respectively, revealing that the interaction of Fe–N_5 active site with H_2O_2 is stronger than that of Fe–N_4 site. The dissociation of one OH* group to generate a reactive •OH is the rate-determining step (RDS), with the free energy increases of 0.34 and 0.72 eV for Fe–N_5 and Fe–N_4 models, respectively. Bader charge analysis shown in Fig. 6c reveals that the 2OH* intermediate accepts electrons of 0.53 and 0.85 |e| from the Fe–N_5 and Fe–N_4 sites, respectively, indicating that the FeN_5/NG has less charge transfer between the adsorbed OH* and the Fe active center. It can be explained that, unlike the Fe–N_4 site in which the Fe atom reaches coordination saturation after adsorption of two OH* groups, the six-coordinated Fe atom can only contribute to the strong tendency for FeN_5 to interact with one single OH* group in the 2OH* step, as the significant difference in charge transfer amount from FeN_5 to the two different OH* groups (0.05 vs 0.48 |e|; Fig. S27). Moreover, the charge transfer from Fe–N_5 site to OH* (-0.42 |e|) is more than that of Fe–N_4site (-0.31 |e|) in the FeN_5/FeN_4-OH* system (Fig. 6d). A significant difference in bonding charge distribution is observed between the Fe atom and surrounding N atoms at the Fe–N_4 and Fe–N_5 sites, which reveal the nature of different charge-transfer properties in the H_2O_2 activation process (Fig. 6e). Therefore, one OH* group is more easily to dissociate from the Fe–N_5 site and then form the free •OH. The enhanced catalytic ability of FeN_5/NG is closely related to its higher ability to adsorb H_2O_2 molecules (larger adsorption energy) and its higher ability to generate •OH (lower energy barrier).

4. Conclusion

In summery, we report a pyrolysis-free and coordination-modulated method to obtain a Fe SAC with axial five-coordinated structure (Fe–N_5) for catalytic oxidation of organic contaminants. The obtained FeN_5/NG is demonstrated to exhibit efficient formation of the active species (mainly •OH), thus showing favorable Fenton activity towards catalytic oxidation of phenol with a degradation rate constant of 0.180 min^{-1}. DFT calculations reveal the dependence of catalytic reactivity on the coordination environment of Fe single-atom, showing that the Fe–N_5 catalytic site more readily adsorbs the H_2O_2 and generates •OH compared to the Fe–N_4 site. Moreover, a novel dual-center mechanism has been proved for understanding the impressive catalytic performance, in which the pyridinic N site on NG serves as the phenol adsorption center and the Fe–N_5 sites serves as the H_2O_2 activation center. Such dual reaction centers facilitate the rapid reaction of •OH generated by H_2O_2 activation with neighboring adsorbed phenol. This work presents a new avenue to regulate the local coordination environment of SACs and establishes the foundation for a detailed understanding of the relationship between the catalyst structure and Fenton activity for further research.

CRediT authorship contribution statement

Haoyang Fu and **Jiaqi Wei**: Conceptualization, Methodology, Software, Data curation, Writing – original draft preparation. **Guangliang Chen** and **Minkai Xu**: Data curation, Writing – original draft preparation. **Jiyuan Liu** and **Jianghong Zhang**: Data curation, Investigation. **Qianyu Xu** and **Yunjie Zou**: Visualization, Investigation. **Ke Li**, **Shibo Xi**, **Xiaodong Chen**, and **Weixian Zhang**: Writing – review & editing. **Lan Ling** and **Shuzhou Li**: Supervision, Conceptualization, Writing – review & editing.

Declaration of Competing Interest

The authors declare that they have no known competing financial interests or personal relationships that could have appeared to influence the work reported in this paper.

Data Availability

The authors do not have permission to share data.

Appendix A. Supporting information

Supplementary data associated with this article can be found in the online version at doi:10.1016/j.apcatb.2022.122012.

References

[1] G. Matafonova, V. Batoev, Recent advances in application of UV light-emitting diodes for degrading organic pollutants in water through advanced oxidation processes: a review, Water Res. 132 (2018) 177–189.

[2] L. Liu, L. Zhou, D. Liu, W. Yuan, S. Chen, H. Li, Z.F. Bian, Z.L. Wang, Improved degradation efficiency of levofloxacin by a self-powered electrochemical system with pulsed direct-current, ACS Nano 15 (3) (2021) 5478–5485.

[3] X. Lu, S. Gao, H. Lin, L. Yu, Y. Han, P. Zhu, W. Bao, H. Yao, Y. Chen, J. Shi, Bioinspired copper single-atom catalysts for tumor parallel catalytic therapy, Adv. Mater. 32 (2020), e2002246.

[4] M. Huo, L. Wang, Y. Wang, Y. Chen, J. Shi, Nanocatalytic tumor therapy by single-atom catalysts, ACS Nano 13 (2019) 2643–2653.

[5] M. Xing, W. Xu, C. Dong, Y. Bai, J. Zeng, Y. Zhou, J. Zhang, Y. Yin, Metal sulfides as excellent co-catalysts for H_2O_2 decomposition in advanced oxidation processes, Chem 4 (2018) 1359–1372.

[6] Y. Zhu, R. Zhu, Y. Xi, J. Zhu, G. Zhu, H. He, Strategies for enhancing the heterogeneous Fenton catalytic reactivity: a review, Appl. Catal. B-Environ. 255 (2019), 117739.

[7] Y. Zhu, R. Zhu, L. Yan, H. Fu, Y. Xi, H. Zhou, G. Zhu, J. Zhu, H. He, Visible-light Ag/ AgBr/ferrihydrite catalyst with enhanced heterogeneous photo-Fenton reactivity via electron transfer from Ag/AgBr to ferrihydrite, Appl. Catal. B-Environ. 239 (2018) 280.

[8] C. Zhang, F. Li, R. Wen, H. Zhang, P. Elumalai, Q. Zheng, H. Chen, Y. Yang, M. Huang, G. Ying, Heterogeneous electro–Fenton using three–dimension NZVI–BC electrodes for degradation of neonicotinoid wastewater, Water Res. 182 (2020), 115975.

[9] J. Tang, J. Wang, Metal organic framework with coordinatively unsaturated sites as efficient Fenton-like catalyst for enhanced degradation of sulfamethazine, Environ. Sci. Technol. 52 (2018) 5367–5377.

[10] J. Wang, K.P. Hou, Y. Wen, H. Liu, H. Wang, K. Chakarawet, M. Gong, X. Yang, Interlayer structure manipulation of iron oxychloride by potassium cation intercalation to steer H_2O_2 activation pathway, J. Am. Chem. Soc. 144 (2022) 4294–4299.

[11] A. Wang, J. Li, T. Zhang, Heterogeneous single-atom catalysis, Nat. Rev. Chem. 2 (2018) 65–81.

[12] L. Jiao, J. Wu, H. Zhong, Y. Zhang, W. Xu, Y. Wu, Y. Chen, H. Yan, Q. Zhang, W. Gu, L. Gu, Densely isolated FeN_4 sites for peroxidase mimicking, ACS Catal. 10 (2020) 6422–6429.

[13] S. Ji, B. Jiang, H. Hao, Y. Chen, J. Dong, Y. Mao, Z. Zhang, R. Gao, W. Chen, R. Zhang, Q. Liang, Matching the kinetics of natural enzymes with a single-atom iron nanozyme, Nat. Catal. 4 (2021) 407–417.

[14] J. Wang, B. Li, Y. Li, X. Fan, F. Zhang, G. Zhang, W. Peng, Facile synthesis of atomic Fe-N-C Materials and dual roles investigation of Fe-N_4 sites in Fenton-like reactions, Adv. Sci. 8 (2021) e2101824.

[15] X. Hai, S. Xi, S. Mitchell, K. Harrath, H. Xu, D.F. Akl, D. Kong, J. Li, Z. Li, T. Sun, H. Yang, Scalable two-step annealing method for preparing ultra-high-density single-atom catalyst libraries, Nat. Nanotechnol. 17 (2022) 174–181.

[16] S. An, G. Zhang, T. Wang, W. Zhang, K. Li, C. Song, J.T. Miller, S. Miao, J. Wang, X. Guo, High-density ultra-small clusters and single-atom Fe sites embedded in

graphitic carbon nitride (g-C_3N_4) for highly efficient catalytic advanced oxidation processes, ACS Nano 12 (2018) 9441–9450.

[17] Z. Guo, Y. Xie, J. Xiao, Z.J. Zhao, Y. Wang, Z. Xu, Y. Zhang, L. Yin, H. Cao, J. Gong, Single-atom Mn–N_4 site-catalyzed peroxone reaction for the efficient production of hydroxyl radicals in an acidic solution, J. Am. Chem. Soc. 141 (2019) 12005–12010.

[18] Y. Luo, Y. Chen, Y. Xue, J. Chen, G. Wang, R. Wang, M. Yu, J. Zhang, Electronic structure regulation of iron phthalocyanine induced by anchoring on heteroatom-doping carbon sphere for efficient oxygen reduction reaction and Al-air battery, Small 18 (2022), e2105594.

[19] X. Zhou, M.K. Ke, G.X. Huang, C. Chen, W. Chen, K. Liang, Y. Qu, J. Yang, Y. Wang, F. Li, H.Q. Yu, Identification of Fenton-like active Cu sites by heteroatom modulation of electronic density, Proc. Natl. Acad. Sci. U.S.A. 119 (2022), e2119492119.

[20] Y. Xiong, H. Li, C. Liu, L. Zheng, C. Liu, J.O. Wang, S. Liu, Y. Han, L. Gu, J. Qian, D. Wang, Single-atom Fe catalysts for Fenton-like reactions: Roles of different N species, Adv. Mater. 34 (2022), e2110653.

[21] S. Liu, D. Liu, Y. Sun, P. Xiao, H. Lin, J. Chen, X.L. Wu, X. Duan, S. Wang, Enzyme-mimicking single-atom FeN$_4$ sites for enhanced photo-Fenton-like reactions, Appl. Catal. B-Environ. 310 (2022), 121327.

[22] T. Chen, Z. Zhu, X. Shen, H. Zhang, Y. Qiu, D. Yin, Boosting peroxymonosulfate activation by porous single-atom catalysts with FeN$_4$O$_1$ configuration for efficient organic pollutants degradation, Chem. Eng. J. 450 (2022), 138469.

[23] F. Chen, X.L. Wu, C. Shi, H. Lin, J. Chen, Y. Shi, S. Wang, X. Duan, Molecular engineering toward pyrrolic N-rich M-N$_4$ (M= Cr, Mn, Fe, Co, Cu) single-atom sites for enhanced heterogeneous fenton-like reaction, Adv. Funct. Mater. 31 (2021), 2007877.

[24] U.I. Kramm, I. Herrmann-Geppert, P. Bogdanoff, S. Fiechter, Effect of an ammonia treatment on structure, composition, and oxygen reduction reaction activity of Fe–N–C, Catal. J. Phys. Chem. C 115 (2011) 23417–23427.

[25] A. Mehmood, M. Gong, F. Jaouen, A. Roy, A. Zitolo, A. Khan, M.T. Sougrati, M. Primbs, A.M. Bonastre, D. Fongalland, G. Drazic, High loading of single atomic iron sites in Fe–NC oxygen reduction catalysts for proton exchange membrane fuel cells, Nat. Catal. 5 (2022) 311–323.

[26] M. Xiao, Y. Chen, J. Zhu, H. Zhang, X. Zhao, L. Gao, X. Wang, J. Zhao, J. Ge, Z. Jiang, S. Chen, Climbing the apex of the ORR volcano plot via binuclear site construction: electronic and geometric engineering, J. Am. Chem. Soc. 141 (2019) 17763–17770.

[27] H. Xiong, A.K. Datye, Y. Wang, Thermally stable single-atom heterogeneous catalysts, Adv. Mater. 33 (2021), e2004319.

[28] Y. Du, Y. Zhu, S. Xi, P. Yang, H.O. Moser, M.B.H. Breese, A. Borgna, J. Synchrotron, XAFCA: a new XAFS beamline for catalysis research, . Radiat. 22 (2015) 839.

[29] G. Kresse, J. Furthmüller, Efficiency of ab-initio total energy calculations for metals and semiconductors using a plane-wave basis set, Comput. Mater. Sci. 6 (1996) 15–50.

[30] P.E. Blöchl, Projector augmented-wave method, Phys. Rev. B 50 (1994) 17953–17979.

[31] J.P. Perdew, K. Burke, M. Ernzerhof, Generalized gradient approximation made simple, Phys. Rev. Lett. 77 (1996) 3865.

[32] S. Grimme, J. Antony, S. Ehrlich, H. Krieg, A consistent and accurate ab initio parametrization of density functional dispersion correction (DFT-D) for the 94 elements H-Pu, J. Chem. Phys. 132 (2010), 154104.

[33] K. Mathew, V.C. Kolluru, S. Mula, S.N. Steinmann, R.G. Hennig, Implicit self-consistent electrolyte model in plane-wave density-functional theory, J. Chem. Phys. 151 (2019), 234101.

[34] Y. Joly, X-ray absorption near-edge structure calculations beyond the muffin-tin approximation, Phys. Rev. B 63 (2001), 125120.

[35] O. Bunău, Y. Joly, Self-consistent aspects of x-ray absorption calculations, J. Phys. Condens. Matter 21 (2009), 345501.

[36] S.H. Joo, A.J. Feitz, D.L. Sedlak, T.D. Waite, Quantification of the oxidizing capacity of nanoparticulate zero-valent iron, Environ. Sci. Technol. 39 (5) (2005) 1263–1268.

[37] R. Cao, R. Thapa, H. Kim, X. Xu, M. Gyu Kim, Q. Li, N. Park, M. Liu, J. Cho, Promotion of oxygen reduction by a bio-inspired tethered iron phthalocyanine carbon nanotube-based catalyst, Nat. Commun. 4 (2013) 2076.

[38] P.J. Wei, G.Q. Yu, Y. Naruta, J.G. Liu, Covalent grafting of carbon nanotubes with a biomimetic heme model compound to enhance oxygen reduction reactions, Angew. Chem. Int. Ed. Engl. 53 (2014) 6659–6663.

[39] Y. Zhu, B. Zhang, X. Liu, D.W. Wang, D.S. Su, Unravelling the structure of electrocatalytically active Fe–N complexes in carbon for the oxygen reduction reaction, Angew. Chem. Int. Ed. 126 (2014) 10849–10853.

[40] W. Liu, L. Zhang, X. Liu, X. Liu, X. Yang, S. Miao, W. Wang, A. Wang, T. Zhang, Discriminating catalytically active FeN$_x$ species of atomically dispersed Fe–N–C catalyst for selective oxidation of the C–H bond, J. Am. Chem. Soc. 139 (2017) 10790–10798.

[41] K.H. Ong. Environmental Quality (Sewage and Industrial Effluents) Regulations, 1979. (1979).

[42] L. Kong, G. Fang, Y. Chen, M. Xie, F. Zhu, L. Ma, D. Zhou, J. Zhan, Efficient activation of persulfate decomposition by Cu$_2$FeSnS$_4$ nanomaterial for bisphenol A degradation: kinetics, performance and mechanism studies, Appl. Catal. B: Environ. 253 (2019) 278–285.

[43] G. Zhang, Z. Wu, H. Liu, Q. Ji, J. Qu, J. Li, Photoactuation healing of α-FeOOH@g-C$_3$N$_4$ catalyst for efficient and stable activation of persulfate, Small 13 (2017), 1702225.

[44] S. Zhu, X. Li, J. Kang, X. Duan, S. Wang, Persulfate activation on crystallographic manganese oxides: mechanism of singlet oxygen evolution for nonradical selective degradation of aqueous contaminants, Environ. Sci. Technol. 53 (2018) 307–315.

[45] L. Xu, J. Wang, Magnetic nanoscaled Fe$_3$O$_4$/CeO$_2$ composite as an efficient Fenton-like heterogeneous catalyst for degradation of 4-chlorophenol, Environ. Sci. Technol. 46 (2012) 10145–10153.

[46] R. Zhu, Y. Zhu, H. Xian, L. Yan, H. Fu, G. Zhu, Y. Xi, J. Zhu, H. He, CNTs/ferrihydrite as a highly efficient heterogeneous Fenton catalyst for the degradation of bisphenol A: the important role of CNTs in accelerating Fe (III)/Fe (II) cycling, Appl. Catal. B-Environ. 270 (2020), 118891.

[47] J. Wang, C. Liu, L. Tong, J. Li, R. Luo, J. Qi, Y. Li, L. Wang, Iron–copper bimetallic nanoparticles supported on hollow mesoporous silica spheres: an effective heterogeneous Fenton catalyst for orange II degradation, RSC Adv. 5 (2015) 69593–69605.

[48] Y. Zhong, X. Liang, Z. He, W. Tan, J. Zhu, P. Yuan, R. Zhu, H. He, The constraints of transition metal substitutions (Ti, Cr, Mn, Co and Ni) in magnetite on its catalytic activity in heterogeneous Fenton and UV/Fenton reaction: From the perspective of hydroxyl radical generation, Appl. Catal. B-Environ. 150–151 (2014) 612–618.

[49] H. Wang, L. Zhang, C. Hu, X. Wang, L. Lyu, G. Sheng, Enhanced degradation of organic pollutants over Cu-doped LaAlO$_3$ perovskite through heterogeneous Fenton-like reactions, Chem. Eng. J. 332 (2018) 572–581.

[50] Y. Zhu, R. Zhu, Y. Xi, T. Xu, L. Yan, J. Zhu, G. Zhu, H. He, Heterogeneous photo-Fenton degradation of bisphenol A over Ag/AgCl/ferrihydrite catalysts under visible light, Chem. Eng. J. 346 (2018) 567–577.

[51] M. Sun, C. Chu, F. Geng, X. Lu, J. Qu, J. Crittenden, M. Elimelech, J.H. Kim, Reinventing Fenton chemistry: iron oxychloride nanosheet for pH-insensitive H$_2$O$_2$ activation. Environ, Environ. Sci. Technol. Lett. 5 (2018) 186–191.

[52] H.D. Rojas-Mantilla, H.D. Ayala-Duran, R.F.P. xNogueira, Nontronite mineral clay NAu-2 as support for hematite applied as catalyst for heterogeneous photo-Fenton processes, Chemosphere 277 (2021), 130258.

[53] X. Miao, H. Dai, J. Chen, J. Zhu, The enhanced method of hydroxyl radical generation in the heterogeneous UV-Fenton system with α-FeOOH as catalyst, Sep. Purif. Technol. 200 (2018) 36–43.

[54] X. Li, X. Huang, S. Xi, S. Miao, J. Ding, W. Cai, S. Liu, X. Yang, H. Yang, J. Gao, J. Wang, Single cobalt atoms anchored on porous N-doped graphene with dual reaction sites for efficient Fenton-like catalysis, J. Am. Chem. Soc. 140 (2018) 12469–12475.

[55] M.K. Rabchinskii, S.D. Saveliev, D.Y. Stolyarova, M. Brzhezinskaya, D.A. Kirilenko, M.V. Baidakova, S.A. Ryzhkov, V.V. Shnitov, V.V. Sysoev, P.N. Brunkov, Modulating nitrogen species via N-doping and post annealing of graphene derivatives: XPS and XAS examination, Carbon 182 (2021) 593–604.

[56] G. Liu, X. Li, P. Ganesan, B.N. Popov, Studies of oxygen reduction reaction active sites and stability of nitrogen-modified carbon composite catalysts for PEM fuel cells, Electrochim. Acta 55 (2010) 2853–2858.

[57] Y. Wang, G. Jia, X. Cui, X. Zhao, Q. Zhang, L. Gu, L. Zheng, L.H. Li, Q. Wu, D. J. Singh, D. Matsumura, Coordination number regulation of molybdenum single-atom nanozyme peroxidase-like specificity, Chem 7 (2021) 436–449.